A computational fluid dynamics (CFD) model for investigating air-pumping mechanisms in air-borne tire noise

Prashanta Gautam[*]
pg37@zips.uakron.edu
Department of Mechanical Engineering
University of Akron
Akron, OH - 44325-3903
USA

Abhilash J. Chandy[**]
achandy@uakron.edu
Department of Mechanical Engineering
University of Akron
Akron, OH - 44325-3903
USA

*Presenter
**Corresponding author

Prashanta Gautam and Abhilash J. Chandy

A computational fluid dynamics (CFD) model for investigating air-pumping mechanisms in air-borne tire noise

ABSTRACT: The reduction in powertrain noise over the last decade has led to an increased focus in reducing tire-road noise, largely due to the environmental concerns related to road traffic noise in industrial countries. Computational Fluid Dynamic (CFD) simulations conducted using ANSYS FLUENT, are presented here with the objective of understanding air-pumping noise generation mechanisms in tire-road contact. The CFD model employs a large eddy simulation (LES) turbulence modeling approach, where the filtered compressible Navier-Stokes equations are solved for two-dimensional (2D) tire geometries, and temporal and spatially accurate pressure fluctuations are utilized to determine sound pressure levels and dominant frequencies. The 2D tire geometry is employed to study the noise effects resulting from single and multiple grooves with prescribed sidewall movement, which represents deformations due to the tire movement on a road surface. Validation of the model is conducted through qualitative and quantitative comparisons with previous computational and industry testing studies. These simulations are intended to provide a deeper understanding about the small-scale noise generation as well as the near- and far-field acoustics, thereby identifying control parameters that can help optimize the tire performance in terms of acoustics through novel and improved designs and paving the way for the automotive manufacturer to compare a variety of tires' noise and vibration characteristics without spending time and money for vehicle pass-by tests.

KEY WORDS: Air pumping, Tire noise, Aero-acoustics, Computational fluid dynamics

Introduction

Traffic noise has a significant contribution towards environmental noise pollution in developed countries due to the presence of a large number of vehicles. Powertrain noise and tire noise form a major part of this vehicle noise. Tire noise is very critical to noise control, since unlike other noise sources, it is relatively difficult to attenuate the tire noise after it is produced [1]. Furthermore, tire noise represents the largest percentage of noise, after engine noise, even under accelerating conditions [2]. Over the last decade, due to the reduction in powertrain noise in vehicles, tire noise control with regards to the overall vehicle noise has received an increased attention.

It is important to have knowledge about the sources of tire noise in order to control them. One should also understand the interactions between the tire and the road in order to fully understand the noise generation mechanisms, which due to their complex nature, require sophisticated models. These mechanisms can be roughly divided into (a) noise generation mechanisms and (b) amplification/reduction mechanisms [3, 4]. The generation mechanisms are further divided into structure-borne and air-borne mechanisms, which are responsible for high frequency and low frequency noise, respectively. Structure-borne noise is caused by mechanical vibrations and tire impact. On the other hand, air-borne noise is caused mainly by air turbulence, resonance effects and the displacement of air when the tire tread comes in contact with the road surface at the tire/road interface. The amplification/reduction mechanisms can influence both structure-borne and air-borne noise. One of the most important amplification mechanisms in tire/road noise is the horn effect, which is caused by the horn-like geometry formed by the tire belt and the road surface. The horn effect influences acoustic wave propagation and can lead to amplifications of upto 10-20 dB [5].

Air-borne noise control in tires has not received as much attention as structure-borne noise in the literature. This is mainly because, experimentally, it is quite difficult to isolate the aerodynamic sources and a lot of care has to be given in order to ensure the obtained data is not polluted by vibration and background noise. However, computationally, this can be achieved using an accurate

numerical model, that can represent the complex phenomenon involved in tire/road interaction and resulting effect on the air. Among air-borne noise generation mechanisms, air pumping is caused by the displacement of air in the pockets between tire tread and road surface [6]. One of the first studies in air pumping mechanism was done by Hayden [7], where he described the mechanism using acoustic monopoles, assuming that the density and pressure fluctuations in the air during air pumping are low. However, Gagen [8,9] argued that due to the sluggish nature of air in responding to changes in volume, there are large density and pressure fluctuations which invalidate the use of monopole theory. He proposed the "squeezed acoustic wave equation" for squeezed cavity systems [8] and later extended it to consider the non-linear effects in air pumping [9]. However, his equation represented a simplified case and still did not take into account the geometrical effects in air pumping and propagation.

A direct computational approach that can be used to analyze noise generation during tire/road interaction is the use of a fluid structure interaction (FSI) solver. This kind of approach involves the coupling of a structural solver, which calculates the structural deformations of a tire and the tire grooves, with a fluid solver, which provides a solution for the resulting effects on the surrounding air. However, limitations in computational resources and modeling complexity limits the use of FSI. An alternative approach is to bypass the use of the structural solver and model deformations instead. Kim *et al.* [10] used such an approach to propose a three-stage hybrid technique for predicting air pumping noise generation. The three steps involved were a small-scale noise generation, near-field noise propagation and far-field noise prediction, where flow properties from one step were used to predict the effects in each successive step. The small-scale noise generation was studied using a piston/sliding-door/cavity geometry and the solution was obtained using the groove as the frame of reference. This approach had a one-way interaction between the different steps of analysis and hence, the effect of tire geometry and flow dynamics on the small-scale pumping were not taken into account.

The current study proposes a new unified methodology for the prediction of air-pumping noise generation in tires, where the small-scale air pumping, horn effect as well as far-field noise are

predicted through a single process. The method consists of a 2D tire with one or more lateral grooves sliding along the tire curvature to represent tire rotation. The grooves undergo volume changes due to prescribed deformations of the side walls when they are close to the tire/road interface and the resulting pumping phenomenon is analyzed along with the near-field and far-field noise at different receiver locations. Two different cases are studied here. The first is a tire with a single groove and the second is a tire with two grooves. The small-scale air pumping is solved considering the combined influences of the rotating tire, deforming groove and presence of the horn geometry on the air. The numerical solution of this problem is obtained using the commercial code ANSYS FLUENT, which is a finite volume based solver for the Navier-Stokes equation. The Ffowcs-Williams and Hawkings (FW-H) acoustic model is additionally solved in order to predict the far-field acoustics. Pressure signals at specific near-field and far-field locations are collected and spectral analysis is done using Fast Fourier Transform (FFT) and Short Time Fourier Transform (STFT) algorithms.

Model for air pumping noise prediction

The model used for the prediction of air pumping consists of a 2D tire geometry with lateral grooves which slide along the tire surface and undergo prescribed deformations. Due to the two-dimensional nature of the study, horn geometry is present only on the upstream and downstream sides of the tire and not on the axial directions. The different stages involved in the modeling process has been schematically shown in Figure 1.

The description of the model is divided into six stages according to the state of the tire groove. In stage I, the tire groove approaches the upstream side of the tire/road interface. Since it is in motion, the air pocket that is present inside the groove is not stationary and has a certain flow property associated with it, as is the case in real scenarios. As the groove approaches the tire/road interface, a prescribed deformation of the groove side walls is triggered, as shown in stage II. The volume changes due to this deformation causes a rise in air pressure and as a result, pumping process is initiated. At the same time, the groove gradually starts to close, as it moves into the contact patch.
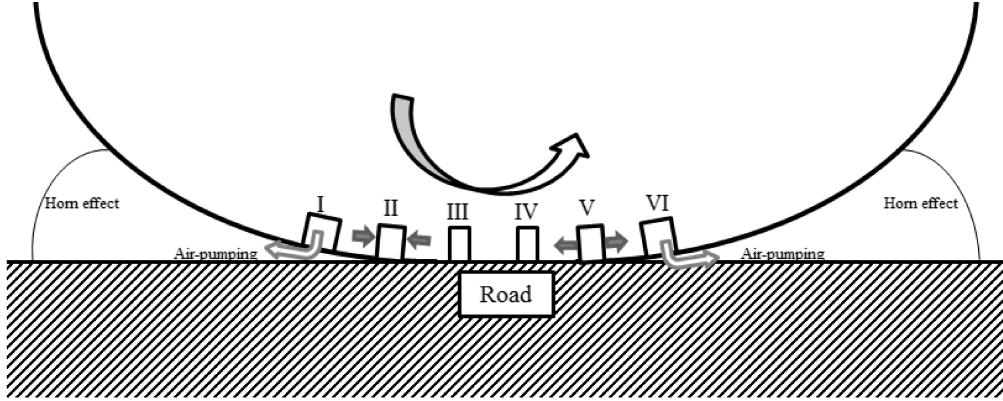
FIG. 1 – *Schematic diagram showing different stages of the tire groove in the prediction model of air pumping noise, along with consideration for horn effect*

Furthermore, the presence of the horn geometry takes into account the horn effect on the upstream side. In stage III, the groove is in the contact patch and there is no deformation prescribed at this stage. The groove moves through the contact patch and approaches the downstream side of the tire/road interface in stage IV. At the beginning of stage V, the groove starts leaving the contact patch and starts to open up, as it is returning to its original shape. The air that is trapped inside the groove at high pressure is suddenly released during this stage. This causes an interruption in the suction of outside air into the cavity although its volume is increasing. This phenomenon has been referred to as Helmholtz resonance phenomenon in some studies [11, 12]. The high pressure air that escapes out from the groove on the downstream side is influenced by the horn geometry. The groove finally reaches its original shape in stage VI. For the far-field acoustic analysis, a control surface is chosen which surround the tire geometry and input for the acoustic model is obtained from this control surface. A solution for the acoustic model is obtained simultaneously while solving the fluid dynamic equations and hence, there are no further solutions stages involved. In order to simulate a tire rolling over a rotating drum like in an experimental setup, ambient air flow is not considered. Furthermore, the road and tire is moving on a common operating velocity (See the Computational Details section for more details). It should be noted that only air-borne noise generation and propagation mechanisms are taken into account using this model.

Governing equations

The air pumping model discussed in the previous section is solved using a set of governing equations for the air. Since the pumping process involves large changes in density and pressure of air, the compressible forms of the governing equations are used for the fluid. However, a complete solution of the fluid, both near-field and far-field is not economical in terms of computational resources and time. Therefore, an acoustic model is used to predict far-field acoustics in air pumping, after the near-field is solved using a direct computational approach. This section discusses the governing equations related to the fluid model as well as the acoustic model.

Computational fluid dynamic (CFD) equations

The compressible forms of the LES-filtered continuity (Eq. (1)) and momentum equations (Eq. (2)) are solved in order to take the compressible properties of air into account and also model the turbulence in the resulting flow.

$$\frac{\partial \rho}{\partial t} + \frac{\partial (\rho \bar{u}_i)}{\partial x_i} = 0 \tag{1}$$

$$\frac{\partial (\rho \bar{u}_i)}{\partial t} + \frac{\partial (\rho \bar{u}_i \bar{u}_j)}{\partial x_j} = \frac{\partial \sigma_{ij}}{\partial x_j} - \frac{\partial \bar{p}}{\partial x_j} - \frac{\partial \tau_{ij}}{\partial x_j} \tag{2}$$

Equation (2) is also called the filtered compressible Navier-Stokes equation where , σ_{ij} is the stress tensor due to molecular viscosity and τ_{ij} is the subgrid-scale (SGS) stress tensor, defined using Boussinesq hypothesis for LES models.

$$\sigma_{ij} = \left[\mu \left(\frac{\partial \bar{u}_i}{\partial x_j} + \frac{\partial \bar{u}_j}{\partial x_i} \right) \right] - \frac{2}{3} \mu \frac{\partial \bar{u}_l}{\partial x_l} \delta_{ij} \tag{3}$$

$$\tau_{ij} - \frac{1}{3} \tau_{kk} \delta_{ij} = -2\mu_t \left(\bar{S}_{ij} - \frac{1}{3} \bar{S}_{kk} \delta_{ij} \right) \tag{4}$$

6

In Eq. (4), μ_t is the SGS turbulent viscosity. For the LES Smagorinsky model, it is defined by,

$$\mu_t = \rho L_s^2 |\bar{S}| \tag{5}$$

In Eq. (5), L_s is the mixing length for the subgrid scale and $|\bar{S}| = \sqrt{2\bar{S}_{ij}\bar{S}_{ij}}$. $\bar{S}_{ij}$ is the strain-rate tensor for the resolved scale, defined by,

$$\bar{S}_{ij} = \frac{1}{2}\left(\frac{\partial \bar{u}_i}{\partial x_j} + \frac{\partial \bar{u}_j}{\partial x_i}\right) \tag{6}$$

For a compressible flow, the filtered energy equation is additionally solved. The air is assumed to be an ideal gas in this study. The filtered energy equation is defined by,

$$\frac{\partial(\rho \bar{h}_s)}{\partial t} + \frac{\partial(\rho \bar{u}_i \bar{h}_s)}{\partial x_j} - \frac{\partial \bar{p}}{\partial t} - \bar{u}_j \frac{\partial \bar{p}}{\partial x_i} - \frac{\partial}{\partial x_i}\left(\lambda \frac{\partial \bar{T}}{\partial x_i}\right) = -\frac{\partial}{\partial x_j}\left[\rho\left(\overline{u_i h_s} - \bar{u}_i \bar{h}_s\right)\right] \tag{7}$$

where, h_s and λ are the sensible enthalpy and thermal conductivity respectively. The subgrid enthalpy flux term on the right side of Eq. (7) is approximated using the gradient hypothesis

$$\left[\rho\left(\overline{u_i h_s} - \bar{u}_i \bar{h}_s\right)\right] = -\frac{\mu_t}{Pr_t}C_p\frac{\partial \bar{T}}{\partial x_j} \tag{8}$$

where, C_p is the specific heat for the fluid and Pr_t is the subgrid Prandtl number.

These governing equations for the fluid are discretized and solved using the finite volume solver in ANSYS FLUENT.

FW-H acoustic model

The acoustic model used in this study is the Ffowcs-Williams and Hawkings (FW-H) model, which is an inhomogeneous wave equation derived from the continuity and Navier-Stokes equations [13].

The FW-H equation is written as

$$\frac{1}{a_0^2}\frac{\partial^2 p'}{\partial t^2} - \nabla^2 p' = \frac{\partial^2}{\partial x_i \partial x_j}\{T_{ij}H(f)\} - \frac{\partial}{\partial x_i}\left[\{P_{ij}n_j + \rho u_i(u_n - v_n)\}\delta(f)\right]$$
$$+ \frac{\partial}{\partial t}\left[\{\rho_0 v_n + \rho(u_n - v_n)\}\delta(f)\right] \tag{9}$$

Here, u_i is the fluid velocity in x_i direction, u_n is the fluid velocity normal to surface $f = 0$, v_i is the surface velocity in x_i direction, v_n is the surface velocity normal to the surface, $\delta(f)$ is the Diract delta function and $H(f)$ is the Heaviside function. The surface $f = 0$ mentioned here is the mathematical surface that embeds the exterior flow problem in an unbounded space in order obtain the solution using the generalized function theory and the free-space Green function. Furthermore, in Eq. (9), n_i is the unit normal vector pointing towards the exterior region, a_0 is the far-field acoustic velocity and p' is the far-field sound pressure. Also, T_{ij} is the Lighthill stress tensor obtained by the relation,

$$T_{ij} = \rho u_i u_j + P_{ij} - a_0^2(\rho - \rho_0)\delta_{ij} \tag{10}$$

P_{ij} in Equations (9) and (10) is the compressive stress tensor, which for a Stokesian fluid is given by,

$$P_{ij} = p\delta_{ij} - \mu\left[\frac{\partial u_i}{\partial x_j} + \frac{\partial u_j}{\partial x_i} - \frac{2}{3}\frac{\partial u_k}{\partial x_k}\delta_{ij}\right] \tag{11}$$

The acoustic wave equation in Eq. (9) is solved using the assumptions that there are no obstacles between the sound source and the receivers, in order to obtain the acoustic pressure due to monopole, dipole and quadrupole sources. In FLUENT, the solution of the FW-H equation can be obtained simultaneously with the CFD equations and acoustic pressure at the receiver locations can be obtained on the fly. Therefore, using the acoustic model in order to predict the far-field acoustics can be done simultaneously and it is also economical compared to a direct solution.

Spectral analysis tools

After the flow properties and acoustic pressure are obtained for the receiver locations, spectral analysis tools are used in order to analyze the sound generated during air pumping. For this purpose, the Fast Fourier Transform (FFT) tool available in FLUENT is used. The FFT tool calculates the power spectral density (PSD) spectrum from the evolution of acoustic pressure, which can then be used to obtain the sound pressure level (SPL) spectrum using the relation,

$$SPL = 10log_{10}\left(\frac{PSD}{P_{ref}^2}\right) \tag{12}$$

In Eq. (12), $P_{ref} = 2 \times 10^{-5} Pa$ is the reference pressure at the threshold of human hearing. Prior to implementing the FFT algorithm, the static offset of the pressure signal is removed using the mean value removal tool. However, no windowing functions are used due to the impulsive nature of the signal. It is common practice to use the A-Weighted SPL spectrum over a 1/3-Octave Band in order to analyze tire noise. The A-Weighted SPL is the SPL weighted by the A-scale function, which closely approximates the frequency response of a human.

Due to the non-stationary nature of the pressure signal, a time variation of the sound is necessary to provide more information. For this purpose, a Short-Time Fourier Transform (STFT) algorithm is used to obtain a spectrogram in Matlab. The STFT algorithm divides the signal into sections and applies Discrete Fourier Transform (DFT) algorithm on each section to obtain the time variation of the frequency spectrum, which can then be plotted to obtain a spectrogram. A windowing function is applied on each section of the signal before DFT and for this purpose, Hanning window is used in this study.

Computational details

The governing equations mentioned in the previous section are solved for a computational model using a set of numerical parameters. The computational model, mesh and numerical parameters used to obtain the numerical solution are discussed in this section. Furthermore, the methodology

for the collection of acoustic data at the near-field and far-field are also discussed here.

Computational geometry and mesh

The diameter of a 215/60R16 tire is considered in the 2D tire geometry for this study. The tire geometry considered here is undeformed. The only difference between the two cases considered in this study, named Case 1 and Case 2 henceforth, are that Case 1 has only one groove while Case 2 has two grooves on the tire. The geometry for both the cases can be seen in Figure 2.
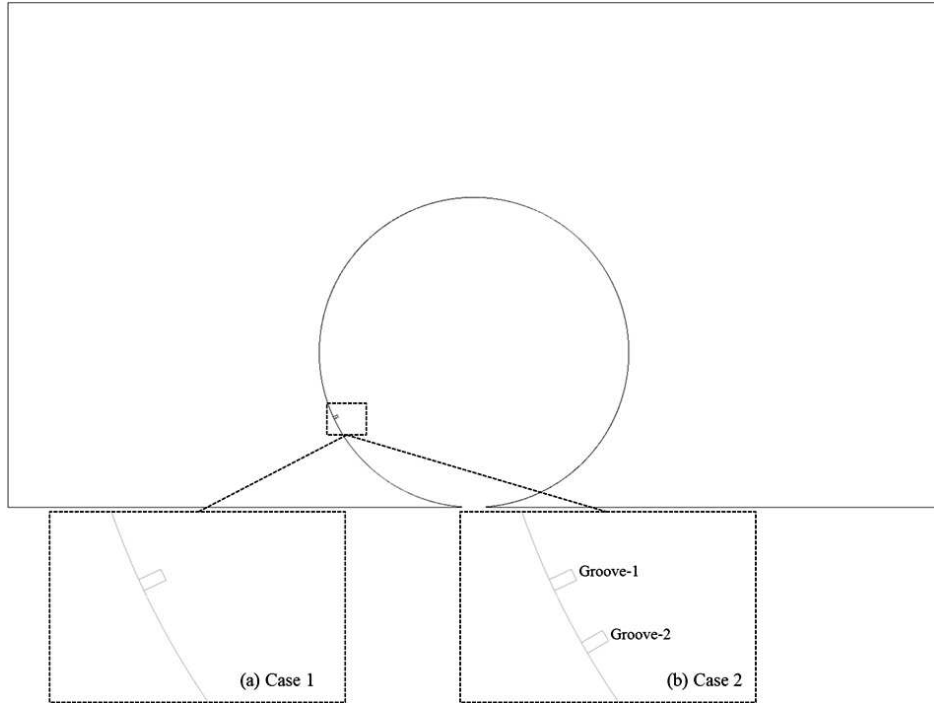

FIG. 2 – *Analysis geometry for 2D tire with dimensions of a 215/60R16 tire, for two different cases, (a) Case 1 with one groove (b) Case 2 with two grooves*

The grooves are of size $5mm \times 10mm$ similar to [14] and are initially placed far away from the contact patch. This is done so that the initial fluctuations generated as the tire starts rotating, is cleared out of the computational domain. For Case 1, the initial position of the groove is at 65° , from the point of tangency of tire with road. For Case 2, groove-1 is at the same position as the groove for Case 1 and groove-2 is placed 5° towards the contact patch, relative to groove-1.

The computational mesh used for this study is shown in Figure 3. The mesh shown in the

figure is for Case 1, and is very similar to Case 2 as well, the only difference being the additional groove. The mesh size near the tire is made up of the similar sized elements so that the near-field pressure fluctuations are resolved accurately. Mesh biasing is used to coarsen the mesh which are farther from the tire, in order to absorb the generated pressure fluctuations before they reach the boundaries. A non-conformal mesh is used between the grooves and tire-exterior domain for both
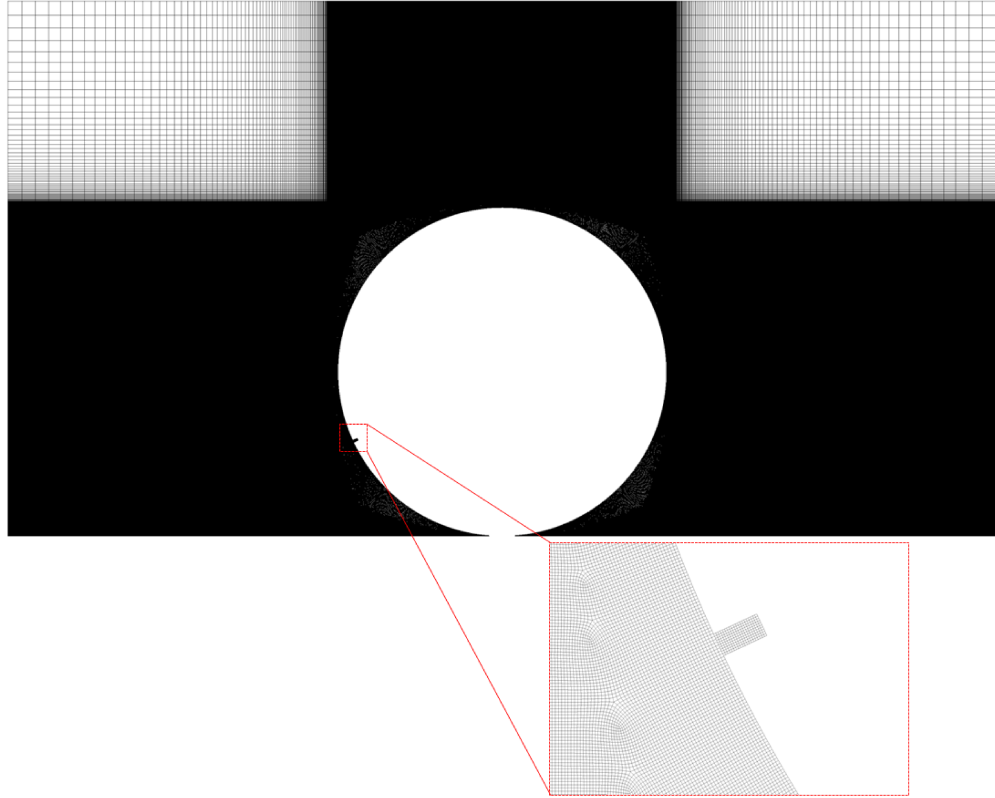

FIG. 3 – *Computational mesh used for the simulation with a close-up view of the meshing near the groove for Case 1*

the cases, in order to enable the use of the sliding mesh technique. Addition of inflation layers on the tire surface is not done to make sure that the size of the non-conformal mesh between the tire surface and the grooves are the same. Instead, the mesh size is made fine around the tire. The cut-out surface at the contact patch results in a good quality mesh with a minimum orthogonal quality of around 0.77.

A mesh independence test is also conducted in order to ensure that the results obtained are spatially accurate. Two cases with 4×10^5 elements and 5.2×10^5 elements are run for Case 2 and

pressure data is collected at different locations. It is found that the maximum difference in pressure values for the main pumping signals are in the range of $5Pa$ and the small amplitude pressure waves captured towards the end of the simulation, after the main pressure wave has already passed, are slightly out of phase. However, due to very small amplitudes compared to the main pressure signal, they will not influence the results noticeably. Thus, it is concluded that the solution is spatially accurate and mesh independent. The results presented here are for 5.2×10^5 mesh elements, most of which are structured.

Numerical parameters and boundary conditions

The parameters used for the simulation are shown in Table 1. The simulation is carried out for a vehicle speed of $40km/hr$. This velocity is used as the boundary condition for the road surface to represent a rotating drum (as in an experiment) and a rotating boundary condition is also used equivalent to the vehicle speed for the tire surface. The prescribed deformations of the groove result in a 23% deformation by volume. Volume monitors in FLUENT are used to analyze the groove deformations.

In order to define the start and end of deformation of the grooves on the upstream and downstream sides, the angular displacement of the grooves are used as triggers. The boundaries surrounding the domain are treated as freestream boundaries so that any pressure fluctuations that are generated pass through them without any reflections. Since the tire grooves start their rotation from a position far away from the contact patch, it is assumed that the domain attains a steady condition before the pumping process begins and there are no background pressure fluctuations which effect the pumping pressure data. So, it can be concluded that the study closely represents an experimental setup inside an anechoic chamber. It should be noted that the parameters for the study, including the prescribed volumetric deformations, are similar to the ones used in the experimental study by Takami *et al.* [15].

For the finite volume solver, a bounded central difference scheme is used for the momentum equations while second order upwind schemes are used for all other equations. Pressure-velocity

coupling is achieved using the PISO scheme. Temporal discretization employs a second order implicit scheme. User defined functions (UDF) are used in order to move and deform the grooves. A non-conformal sliding mesh technique is used in order to rotate the grooves along the tire surface. Similarly, layering technique is used to change the mesh during groove deformation.

Collection of near-field and far-field acoustic data

Spectral analysis is conducted for pressure data collected at various near-field and far-field receiver locations (Table 2) in order to study how the noise characteristics change as the acoustic waves propagate through the computational domain. Some of the receiver locations are similar to the experimental study by Takami *et al.* [15]. For consistency, these receivers are named receivers 1, 3, 9 and 11, similar to their paper. Since this study only involves two-dimensional cases, only the receivers which fall on the symmetry plane of the tire are used from the experiment. Furthermore, in order to study acoustic properties at locations farther away from the tire, two receiver locations 2 and 4 are additionally used. Therefore, there are six receivers in total, three each, on the upstream and downstream sides of the tire.

The near-field receiver locations fall inside the control surface (the red-line in the figure), as shown in Figure 4 and the pressure data for these locations are obtained through direct computation. The far-field receivers fall outside the computational domain and directly solving for air pressure at these locations requires a huge amount of computational resources. Consequently, the control surface is used as the source for the FW-H acoustic model. Pressure data at every 50 time steps is collected at the receiver locations for both cases 1 and 2 for a simulation time interval of 0.03 s, and spectral analysis is done using the FFT tool in FLUENT and STFT algorithm in Matlab. This results in a frequency resolution of around 34 Hz and a sampling frequency of 20 kHz.

Results and discussion

In this section, the results obtained from the simulation for the two cases mentioned in the previous sections are discussed. The propagation of pressure waves along the horn geometry in the upstream
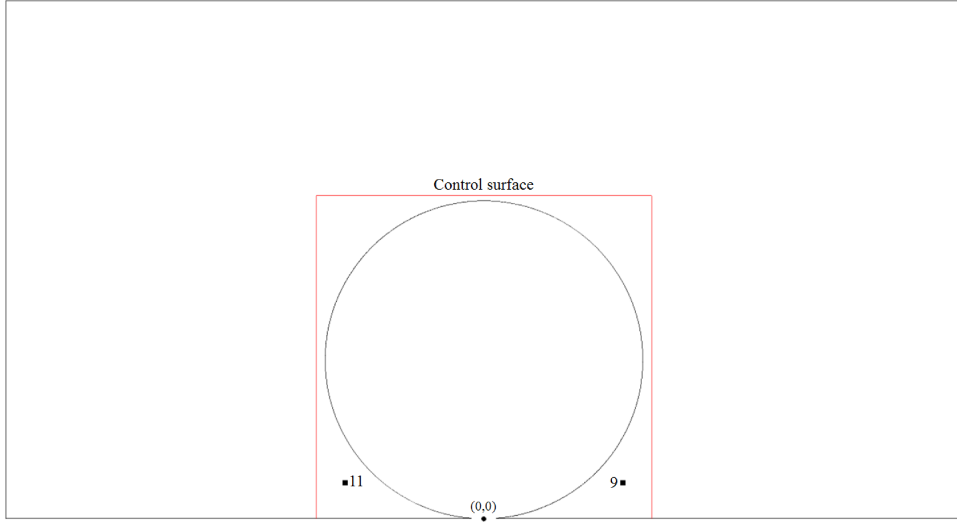
FIG. 4 – *Details related to collection of acoustic data*

and downstream sides of the tire for Case 2 is discussed using instantaneous pressure contours along with close-up views of the grooves. The close-up views are used to show the different stages that the grooves undergo at the tire/road interface. Furthermore, results obtained from the spectral analysis of the two cases are discussed in order to study the sound generated at near-field and far-field receiver locations.

Pressure Contours

The pressures contour showing the propagation of pressure waves generated due to air pumping on the upstream and downstream sides of the tire in Case 2 are shown in Figure 5. The figure also contains close-up views of the grooves at the tire/road interface in order to show the different stages that the grooves undergo in the proposed model. Since the pressure contours for Case 1 does not provide any additional details regarding the propagation of acoustic waves through the horn geometry, they are not shown here.

Figure 5a shows the instantaneous pressure contour generated due to air pumping when the grooves are moving through the tire/road interface, on the upstream side. The deformed shape of groove-2 and the undeformed groove-1 can be seen in the close-up view. When compared to the
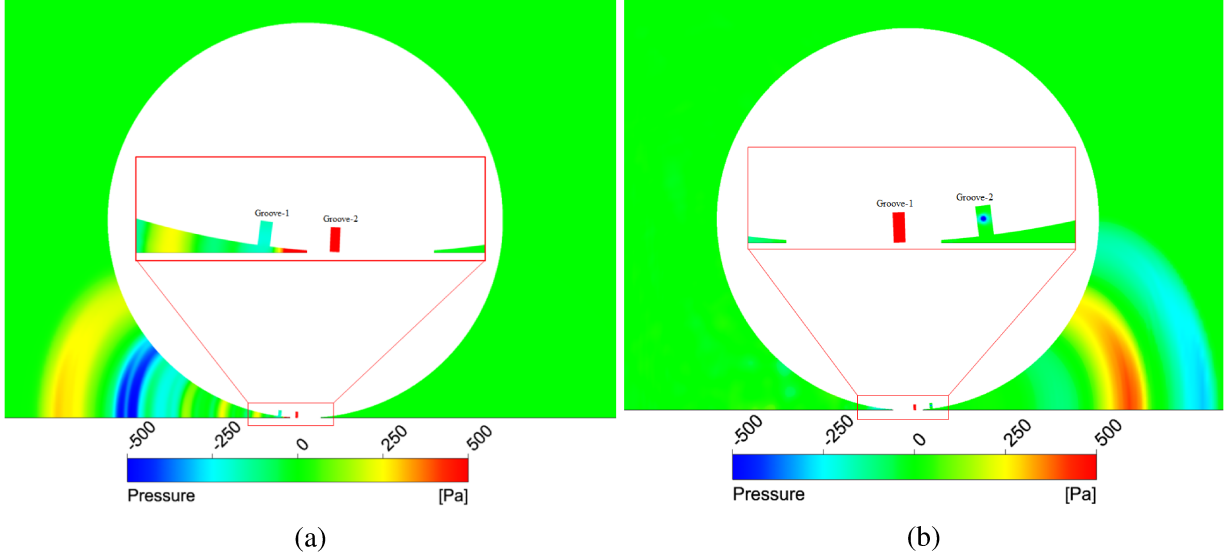
FIG. 5 – *Instantaneous pressure contour showing propagation of pressure waves through horn geometry for Case 2 when the grooves are at (a) the upstream side of the tire (b) the downstream side of the tire*

schematic diagram in Figure 1, groove-1 is at stage I while groove-2 is at stage III. The pressure waves that are seen in the figure are therefore generated due to the deformation of groove-2. It can be seen that the air at high pressure is trapped inside groove-2. Since the analysis is 2D in nature, this high pressure air only escapes out when the grooves open up at the downstream side. However, in a real 3D simulation scenario, sound is generated in the axial direction of the tire as well, giving rise to a directivity pattern in air pumping noise. It can be seen that the pressure waves generated due to the deformation of the grooves are modified due to the horn geometry in the upstream direction.

Figure 5b shows the propagation of the pressure waves through the horn geometry in the downstream side of the tire, along with a close-up view of the two grooves. When compared to Figure 1, groove-1 is at stage IV while groove-2 is at stage VI. The pressure waves traveling through the horn geometry occur due to the release of the high pressure air from groove-2 as it opens up on the downstream side. Furthermore, groove-2 also returns back to its original shape as it leaves the tire/road interface. Also, the horn effect is something that is caused due to the horn geometry in both the upstream and downstream sides of the tire. It can be seen from the pressure diagrams that

the pressure waves generated from the grooves travel through the horn geometry and this influences the noise propagation.

Influence of additional groove on pressure signal

Since the calculations presented here involve the modeling of the generation and propagation of air pumping noise in a single stage, the influence of placing multiple grooves in a tire, on the propagation of acoustic waves through the horn geometry can also be studied. The influence of the additional groove present in Case 2, compared to Case 1 on the propagation of the pressure waves through the horn geometry is studied using the evolution of the pressure signal with time at the near-field receiver 11, as shown in Figure 6.

(a)   (b)
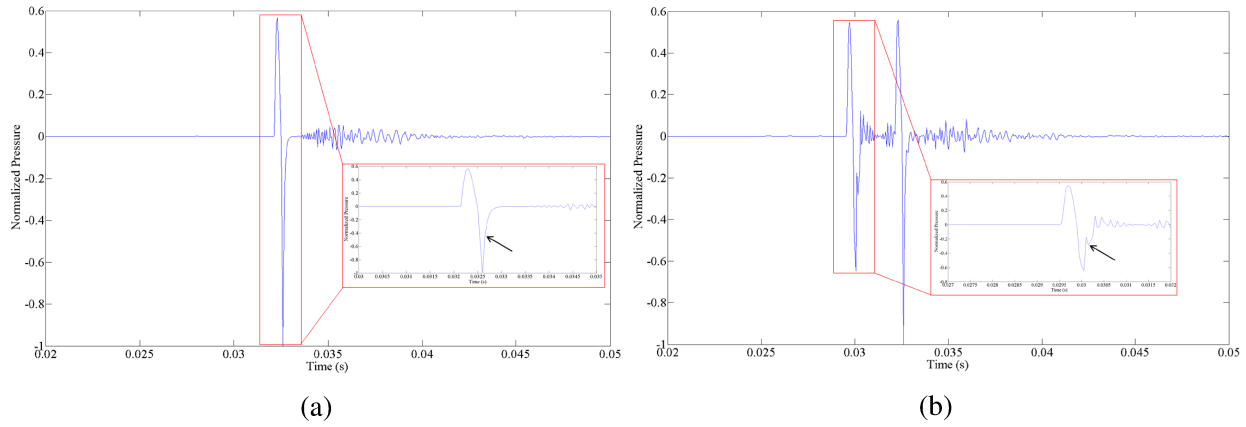
FIG. 6 – *Comparison of pressure evolution at receiver 11 for the different cases studied (a) Case 1 (b) Case 2*

The pressure evolution diagram for Case 1 (Figure 6a) shows one distinct pressure wave generated due to air pumping by the single tire groove. On the other hand, the pressure evolution for Case 2 (Figure 6b), shows two distinct pressure waves, generated due to the pumping effect of the two grooves present in the tire. The first pressure wave is generated due to groove-2 while the second is generated due to groove-1. In the close-up view of the pressure wave due to groove-2, a secondary minimum (shown by the arrow-head) can be seen after the primary minimum. However, when the close-up view of the pressure wave in groove-1 (Figure 6a), the secondary wave is not

present. It can be seen in Figure 5 that groove-1 is a part of the upstream horn geometry when the pressure waves generated by groove-2 propagates. However, the horn geometry for Case 1 is formed only by the smooth tire curvature. Therefore, it can be inferred that the secondary wave visible in the pressure evolution diagram in Figure 6b is generated due to the presence of a groove in the horn geometry.

Furthermore, when the two primary pressure waves in Figure 6b are compared, it can be seen that the first pressure wave is of a smaller magnitude than the second wave. However, the nature of the second pressure wave is similar to the primary wave for Case 1, seen in Figure 6a. This can also be attributed to the presence of the additional groove on the horn geometry when the pumping pressure wave due to groove-2 propagates. The change in the nature of the pressure signal can alter the spectral characteristics of the air pumping noise and this is discussed in the following sections.

Acoustic characteristics of tire with one groove

The near-field and far-field receivers are used to study the spectral characteristics of the generated noise as the pressure waves generated by air pumping propagates. The one-sided 1/3-Octave band spectrum of the A-weighted SPL at the different receiver locations for Case 1 can be seen in Figure 7. Kim *et al.* [10] reported that most of the energy in air pumping is concentrated in the range of 2-8 kHz. This can also be seen in the SPL spectrum. The decay of acoustic energy with distance is evident from the frequency spectrum since the SPL values decrease as the receiver locations are farther away from the tire. Furthermore, it can be seen that most of the energy is concentrated at a frequency band of 2 kHz for the near-field receivers. As the sound propagates to the far-field locations, the concentration of energy in this band gradually diffuses and the spectrum is of a more broadband type.

In order to study the frequency spectrum in more detail, the STFT algorithm is used to obtain spectrograms for the pressure signal at the receivers. The spectrograms for this case are shown in Figure 8. The colored contour in the spectrograms represent the acoustic energy associated with the noise. The diagrams on the left column are for the upstream receiver locations 11, 1 and 2 while
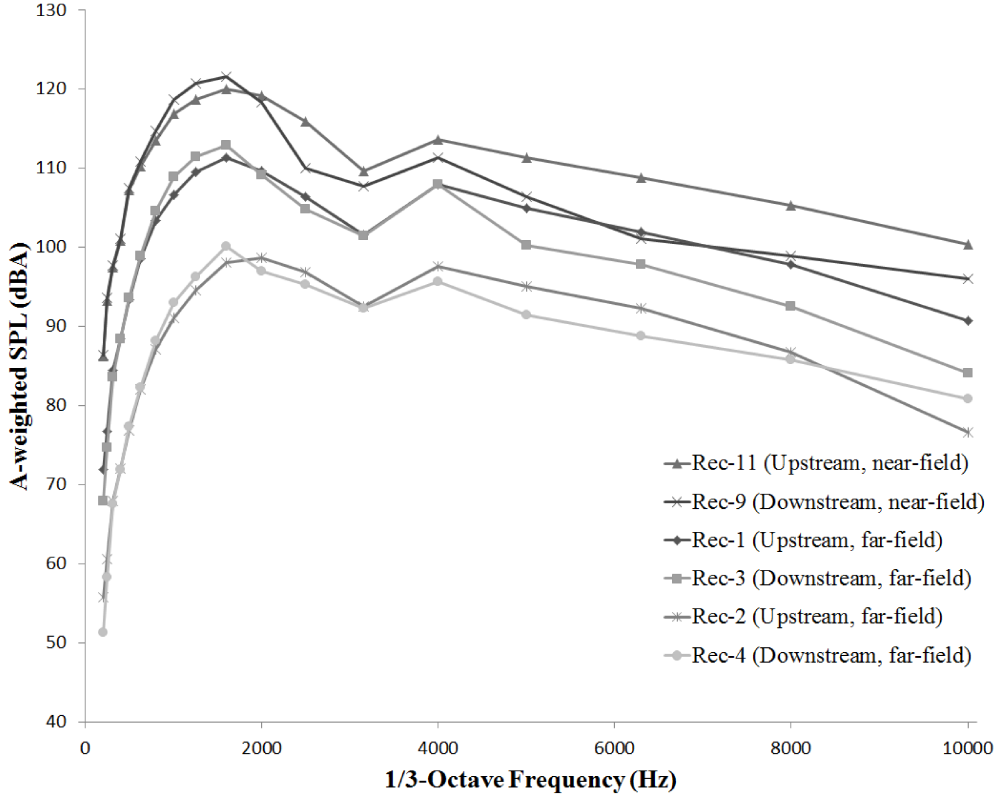
FIG. 7 – *A-weighted SPL spectrum for tire with single groove at near-field and far-field receivers*

the ones on the right column are for the downstream receivers 9, 3 and 4. Thus, the change in the nature of pumping noise as it travel through the air can be studied comparatively from the first row to the last in each column. The spectrograms contain one distinct color band corresponding to the primary pressure wave generated due to the tire groove. It can be seen in Figure 8a that the acoustic energy is concentrated at the range of 2 kHz, which was also seen in the SPL diagram. A higher mode in the range of 4 kHz can also be seen in the spectrogram. The higher mode is not visible in the downstream near-field receiver 9 (Figure 8b). As the receiver locations are farther away, higher frequencies start to appear in the color bands as their significance in the overall acoustic spectrum increases. This was also seen in the SPL spectrum. At receiver 2, a third frequency mode can be seen at around 8 kHz. Thus, the transition to a broadband nature of pumping sound on the far-field receivers, which was seen in the SPL diagrams (Figure 7) is also seen in the spectrograms.
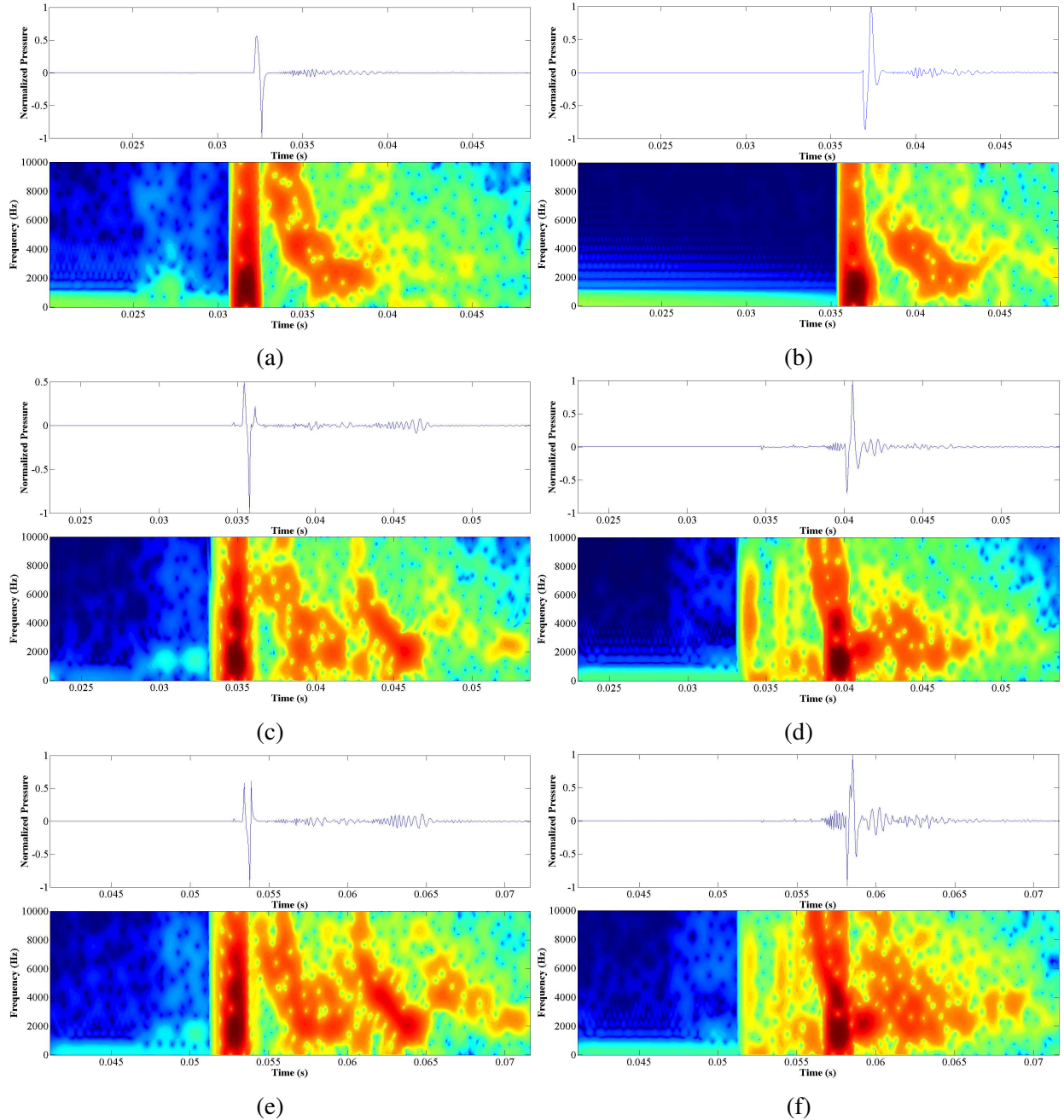
FIG. 8 – *Spectrogram showing time variation of frequency distribution for tire with a single groove at near-field and far-field receiver locations (a) Receiver 11 (b) Receiver 9 (c) Receiver 1 (d) Receiver 3 (e) Receiver 2 (f) Receiver 4*

The one-sided 1/3-Octave band spectrum of the A-weighted SPL at the different receiver locations for Case 2 can be seen in Figure 9. Due to the presence of two grooves, the acoustic energy is
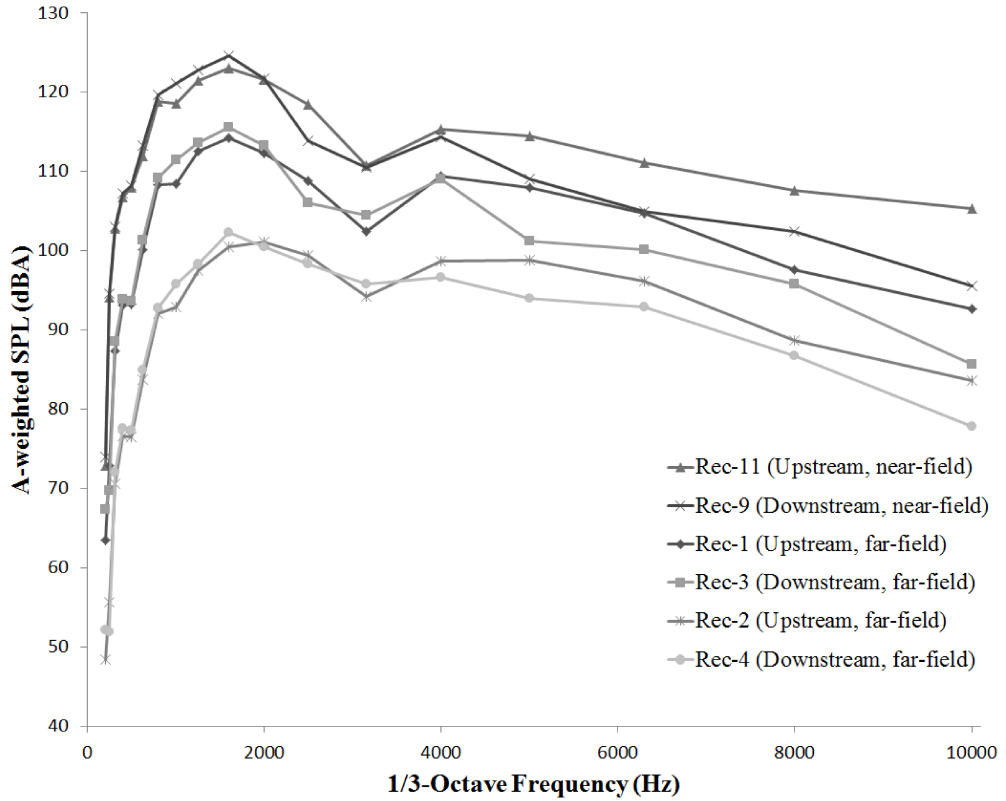

FIG. 9 – *A-weighted SPL spectrum for tire with two grooves at near-field and far-field receivers*

higher than Case 1. However, the nature of decay of the sound with distance is similar to Case 1.

The spectrograms shown in Figure 10 provide more details on the nature of the sound and the influence of the additional groove in this case. The diagrams on the left column are for the receiver locations on the upstream side of the tire while those on the right column are for the receiver locations on the downstream side of the tire. The presence of two grooves in the tire implies that there are two distinct color bands, corresponding to the two primary pressure signals at different times. Distinct dark bands in the range of 2 kHz can be seen, corresponding to the peaks in pressure signal. As discussed previously, the presence of a groove in the horn geometry changes the nature of the pressure signal at the receivers. The corresponding change in the spectral
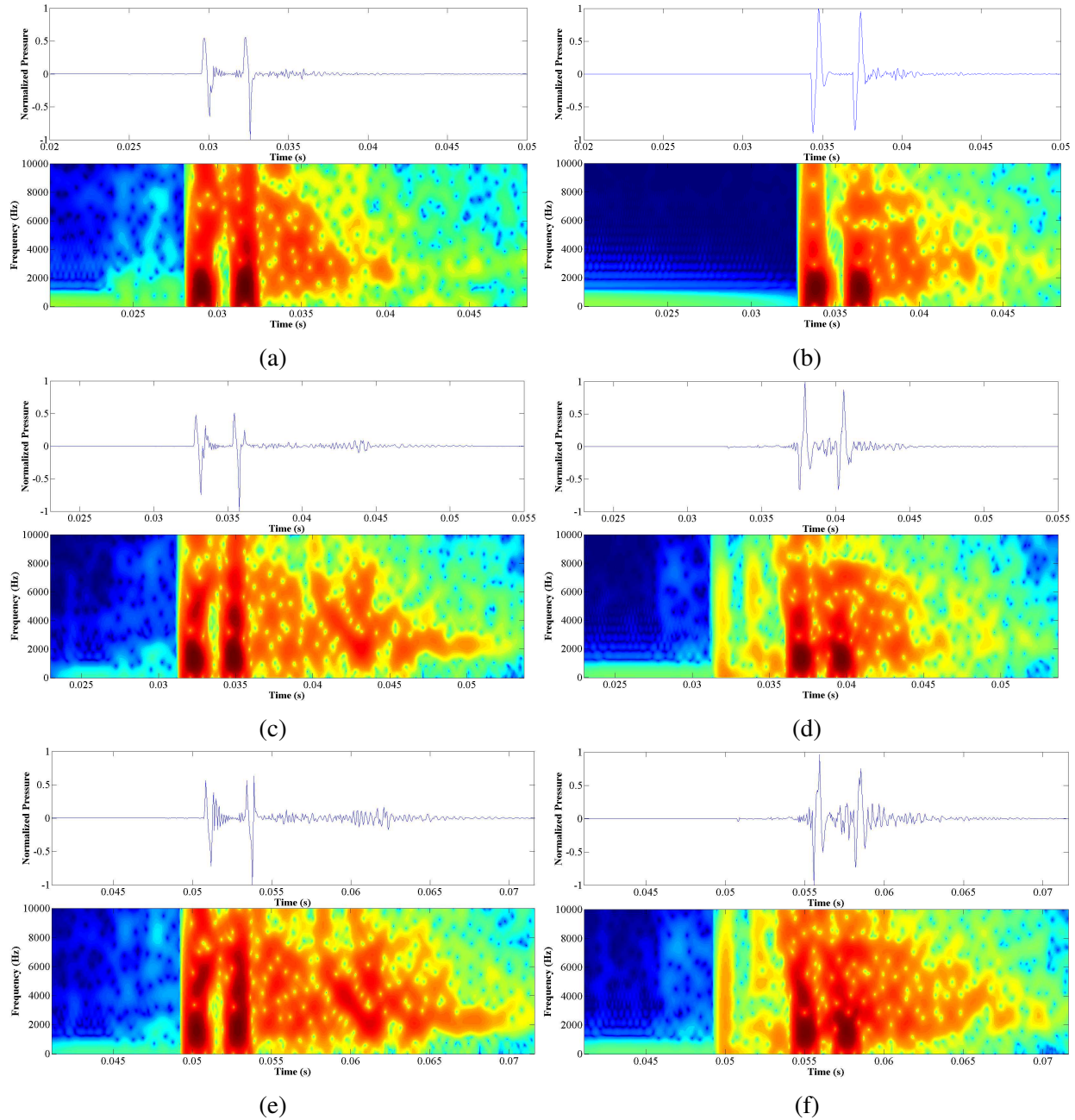
FIG. 10 – *Spectrogram showing time variation of frequency distribution for tire with two grooves at near-field and far-field receiver locations (a) Receiver 11 (b) Receiver 9 (c) Receiver 1 (d) Receiver 3 (e) Receiver 2 (f) Receiver 4*

characteristics can be observed by comparing the two color bands. It can be seen that the whenever there is a groove present in the horn geometry, the acoustic energy for higher frequencies are less pronounced. On the other hand, when the horn geometry is a smooth curvature, the pressure signals are not affected. Consequently, the second band for the upstream receivers and first band for the downstream receivers are similar to the bands seen in the corresponding receiver spectrograms for Case 1.

Conclusion

A unified model for the simulation of air pumping noise generation and propagation is proposed here. The proposed model is described using several stages of the grooves along the tire/road interface and these stages are illustrated in the numerical solution. The numerical solution for the model is obtained using the finite volume solver and FW-H acoustic model in the commercial software, ANSYS FLUENT, where groove deformations are prescribed through UDFs. The results for a tire with (a) one groove and (b) two grooves are presented in order to study the influence of the additional groove in tires. Pressure signals at different near-field and far-field receiver locations are obtained using direct simulations and by using the FW-H acoustic model, and spectral characteristics is used to study the air pumping sound generation and propagation mechanisms.

Since the solution for all scales of air pumping was obtained in a single stage, it was possible to study the interaction between the noise generation mechanisms and propagation mechanisms using this model. It was found that the presence of the additional groove in the tire slightly changes the acoustic characteristics of air pumping. Furthermore, as the receiver locations move farther away, it was found that the noise changes into a more broadband type, with most of the energy concentrated in the range of 2-8 kHz, which is consistent with previous reports [4, 10]. Due to the two-dimensional nature of the simulation, the directivity pattern of air pumping cannot be studied. Other important aspects involved in tire rotation such as flow dynamics due to motion of the grooves, tire/road interaction and irregularities in horn geometry due to grooves can be taken into account through this model. However, the proposed method paves the way for a unified

model in 3D, where all the important aspects of air pumping can be studied and applied in order to optimize tire acoustics through CFD.

References

[1] Heckl, M., 1986. "Tyre noise generation". *Wear,* **113**(1), pp. 157–170.

[2] Iwao, K., and Yamazaki, I., 1996. "A study of the mechanism of tire/road noise". *JSAE Review,* **17**, pp. 139–144.

[3] Sandberg, U., and Ejsmont, J., 2002. *Tyre/Road Noise Reference Book.* INFORMEX, Harg, SE-59040 Kisa, Sweden.

[4] Eisenblaetter, J., Walsh, S., and Krylov, V., 2010. "Air-related mechanisms of noise generation by solid rubber tyres with cavities". *Applied Acoustics,* **71**, pp. 854–860.

[5] Graf, R., Kuo, C.-Y., Dowling, A., and Graham, W., 2002. "On the horn effect of a tyre/road interface, part i: Experiment and computation". *Journal of Sound and Vibration,* **256**(3), pp. 417–431.

[6] Braun, M., Walsh, S., Horner, J., and Chuter, R., 2013. "Noise source characteristics in the iso 362 vehicle pass-by noise test: Literature review". *Applied Acoustics,* **74**, pp. 1241–1265.

[7] Hayden, R., 1971. "Roadside noise from the interaction of a rolling tire with the road surface". *Proceedings of Purdue Noise Contr Conf*, pp. 62–67.

[8] Gagen, M., 1999. "Novel acoustic sources from squeezed cavities in car tires". *J. Acoust. Soc. Am.,* **106**(2), pp. 794–801.

[9] Gagen, M., 2000. "Nonlinear acoustic sources in squeezed car tyre cavities". *Noise & Vibration Worldwide,* **31**(4), pp. 9–19.

[10] Kim, S., Jeong, W., Park, Y., and Lee, S., 2006. "Prediction method for tire air-pumping noise using a hybrid technique". *J. Acoust. Soc. Am.,* **119**(6), pp. 3799–3812.

[11] Hamet, J., Deffayet, C., and Pallas, M., 1990. "Air pumping phenomena in road cavities". *Proceedings of INTROC,* **90**, pp. 19–29.

[12] Nilsson, N., 1979. "Air resonant and vibrational radiation – possible mechanisms for noise from cross-bar tires". *Proceedings of INTROC*, pp. 93–109.

[13] ANSYS, INC., 2014. *ANSYS Academic Research, Help System, ANSYS Fluent Users Guide*, Release 15.0.7 ed.

[14] Gautam, P., and Chandy, A., 2015. "Understanding tire acoustics through computational fluid dynamics (CFD) of grooves with deforming walls". *Proceedings of Internoise 2015/ASME NCAD Meeting (In Publication).*

[15] Takami, K., and Furukawa, T., 2015. "Study of tire noise characteristics with high-resolution synchronous images". *Proceedings of EURONOISE*, pp. 2113–2118.

[16] Winroth, J., 2013. "Dynamic contact stiffness and air-flow related source mechanisms in the tyre/road contact". *Thesis (Chalmers University of Technology).*

[17] Van Keulen, W., and Duškov, M., 2005. "Inventory study of basic knowledge on tyre/road noise". *Delft, Nizozemska, oktober.*

List of Figures

List of Tables

TABLE 1 – *Details for boundary conditions and simulation parameters*

Parameter	Value
Tire size	215/60R16
Vehicle velocity	40 km/hr
Groove dimensions	$5mm \times 10mm$
Volume deformation	23 %
Groove separation value (Case 2)	$5^o (\approx 29mm)$

TABLE 2 – *Coordinate locations of near-field and far-field receivers for collection of acoustic pressure data*

Receiver	Position (mm,mm)
11 (near-field, upstream)	(-290,75)
1 (far-field, upstream)	(-1330,390)
2 (far-field, upstream)	(-7500,500)
9 (near-field, downstream)	(290,75)
3 (far-field, downstream)	(1330,390)
4 (far-field, downstream)	(7500,500)